JACS Au
AN OPEN ACCESS JOURNAL OF THE AMERICAN CHEMICAL SOCIETY

pubs.acs.org/jacsau
Article

Guest-Induced Conformational Transformations in Tiara[5]arene Crystals: A Pathway for Molecular Sieving[⊥]

Zezhao Xu,[‖] Weiwei Yang,[‖] Huiyu Liu, Shan Jiang,* and Andrew C.-H. Sue*

Cite This: *JACS Au* 2024, 4, 3475−3483

Read Online

ACCESS | Metrics & More | Article Recommendations | Supporting Information

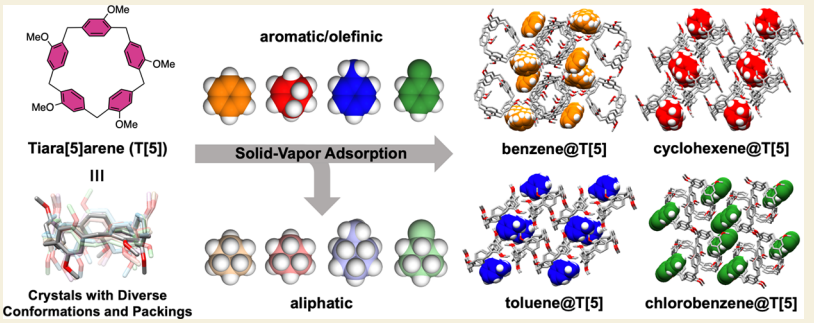

ABSTRACT: In pursuit of environmental sustainability and energy efficiency, assorted macrocyclic compounds have recently emerged as crystalline adsorbents for the efficient molecular sieving of various chemical commodities. Herein, we delve into the conformational characteristics and solid-state packing modes of tiara[5]arenes (**T[5]**), a rim-differentiated pillar[5]arene derivative. By meticulously exploring the conformational space, we have successfully identified a multitude of distinct **T[5]** conformers within a relatively narrow energy range of 22 kJ/mol. This finding underscores the inherent conformational flexibility of this macrocyclic scaffold, enabling **T[5]** to adapt diverse packing arrangements in the solid state. While solvent-free **T[5]** crystals do not exhibit permanent porosity, they undergo solvomorphic interconversions when exposed to various guest compounds. Our study demonstrates that **T[5]**-based crystalline materials exhibit a notable preference for selectively capturing aromatic and olefinic solvents, such as benzene, toluene, chlorobenzene, and cyclohexene, over their aliphatic hydrocarbon counterparts from equivalent volume liquid mixtures, achieving up to 10:1 selectivity between benzene and cyclohexane.

KEYWORDS: *tiara[5]arene, conformational search, host−guest analysis, adsorptive separation*

1. INTRODUCTION

Supramolecular chemistry delves into the intricate world of noncovalent weak forces governing interactions between molecular entities.[1,2] Beyond its critical role in unraveling the delicate interactions underpinning biological systems, recent years have witnessed a burgeoning fascination with harnessing these principles to engineer artificial supramolecular materials.[3−6] These materials hold tremendous promise across a range of applications, including molecular separation, catalysis, biomedicine, electronic devices, and energy storage materials.[7−10] One class of key members that has risen to prominence within this paradigm is macrocyclic compounds.[11−15] Renowned for their innate abilities to form well-defined host−guest complexes, these compounds have garnered significant attention by virtue of their structural diversity and functionality. Apart from their intrinsic pores allowing for precise control over molecular recognition events, on account of their unique shapes and symmetries, they also serve as fundamental building blocks for the construction of molecular cages and framework materials that possess extrinsic porosity.[16−20] Intriguingly, certain crystalline organic materials formed by calixarenes even display the so-called "porosity without pores".[21] Despite lacking atomic-scale channels to interconnect the lattice voids formed by the packing of the macrocycles, these materials allow the permeation of gas and liquid guests, facilitating single-crystal to single-crystal transformations toward inclusion compounds.[22,23]

Recent advancements in pillararene chemistry[24−28] have ushered in new aspects for the development of macrocycle-based crystalline functional materials.[29−32] Both pillar[5]arenes and pillar[6]arenes have played pivotal roles in the construction of assorted supramolecular-organic frameworks (SOFs) exhibiting either intrinsic or extrinsic porosities for selective gas adsorption properties.[33−35] On the other hand, in alignment with the "porosity without pores" concept, crystals

Received: April 5, 2024
Revised: June 24, 2024
Accepted: June 25, 2024
Published: July 9, 2024

https://doi.org/10.1021/jacsau.4c00310
JACS Au 2024, 4, 3475−3483

of pillar[5]arene and pillar[6]arene derivatives, even in the absence of lattice voids, show structural adaptivity and can accommodate specific guest molecules. These nonporous adaptive crystals (NACs) have showcased significant potential in the adsorptive separation of petrochemical commodities.[36,37] For instance, the NACs of pillararenes have shown high selectivity in adsorbing volatile aromatic hydrocarbons over their cyclic aliphatic counterparts,[38−40] as well as in capturing linear alkanes as opposed to branched ones.[41−45]

Understanding the structure−property interplay is essential to advance further research into novel macrocycle-based functional materials. In the context of NACs, the structural flexibility inherent to the macrocyclic scaffold is poised to exert a substantial impact. This innate adaptability empowers these macrocycles to assume diverse conformations or configurations during interactions with various guest molecules and to conform to distinct packing arrangements within the crystalline lattice. As a result, these NACs can undergo energetically favorable solid-state structural transformations while achieving highly selective guest inclusions.

The pillar[5]arene macrocyclic scaffold, e.g., permethylated pillar[5]arene (**P**[**5**], Figure 1), is not entirely rigid; rather in

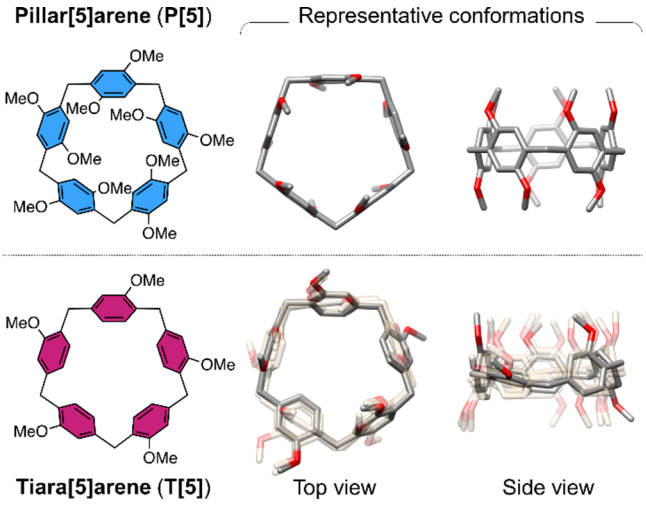

Figure 1. Chemical structures and representative conformations of permethylated pillar[5]arene (**P**[**5**]) and tiara[5]arene (**T**[**5**]) macrocycles, respectively. While **P**[**5**] typically forms "pillar-like" conformers in the solid state, the aromatic panels of **T**[**5**] often exhibit more distorted conformations within the crystal lattice. The cavity diameter of **T**[**5**] is 4.2 ± 0.2 Å, compared with **P**[**5**] is 5.1 Å. The cavity size calculation method can be found in Supporting Information.

solution, the aromatic units within **P**[**5**] can undergo rotational movements around the single bonds of the methylene bridges, a phenomenon often referred to as "*O*-through-the-annulus" circumrotation.[46,47] These movements significantly influence the conformational and stereochemical characteristics of **P**[**5**]. In contrast, in the solid state, **P**[**5**] typically adopts "pillar-like" conformations (Figure 1),[24] where all aromatic units align perpendicularly to the macrocyclic aperture. This arrangement effectively minimizes steric interactions between the alkoxy groups on the rims and allows for the accommodation of solvent guests within the pore.

Recently, our research group introduced a rim-differentiated pillar[5]arene derivative, known as permethylated tiara[5]-arene (**T**[**5**]) (Figure 1), achieved by selectively removing five alkoxyl substituents from one rim. **T**[**5**] exhibits distinctive conformational characteristics compared to **P**[**5**].[48−51] In the crystal lattice, **T**[**5**] often assumes highly distorted conformations with low symmetry,[50] a consequence of this structural modification that grants greater rotational freedom to the **T**[**5**] aromatic units around the methylene groups (Figure 1). Furthermore, under varying crystallization conditions, **T**[**5**] can adopt a plethora of conformations and packing arrangements in the solid state. This inherent flexibility allows **T**[**5**] to adopt a diverse array of conformers within a relatively narrow energy range, a feature not as pronounced in **P**[**5**]. The extensive range of conformational possibilities, coupled with diverse polymorphs in the solid state, positions **T**[**5**] as an excellent candidate for molecular sieving. Our findings indicate that **T**[**5**]'s nonporous crystalline materials have proven to be adaptable and reusable, showing good performance in selectively capturing aromatic and olefinic solvents from mixtures with equal volumes.

In this study, our primary objectives are two-fold: first, to investigate the conformational characteristics of **T**[**5**] in direct comparison with **P**[**5**] through an extensive conformational search analysis; second, to explore the practical utility of **T**[**5**] crystals in accommodating guest molecules. Our computational investigations reveal a compelling contrast: the **T**[**5**] scaffold exhibits a remarkable capacity to adopt a diverse array of conformers, all within a relatively narrow energy range of 22 kJ/mol, whereas **P**[**5**] presents conformers dispersed across a broader energy spectrum of 40 kJ/mol. This inherent flexibility and dynamism suggest that **T**[**5**] has the potential to serve as a pivotal component in adaptive solid-state systems, demonstrating responsive behavior to guest molecules. To experimentally scrutinize the guest-mediated solvomorphic structural transformations, **T**[**5**] was cocrystallized with several benzene derivatives as guest molecules, each inducing distinct alteration in the packing modes of the resulting crystalline material. Notably, solvent-free **T**[**5**] crystals displayed exceptional selectivity in capturing aromatic and olefinic solvents from their equivolume mixtures with corresponding aliphatic compounds. Our findings underscore the profound conformational flexibility of **T**[**5**], illuminating its promise as a dynamic and responsive element in the fields of crystal engineering and molecular separation applications.

2. RESULTS AND DISCUSSION

2.1. Structural Analysis of T[5] Solvomorphic Co-Crystals

Single cocrystals of **T**[**5**] with benzene (BZ), cyclohexene (CHE), toluene (TOL), and chlorobenzene (CBZ) were successfully obtained by subjecting their respective solutions to slow vapor evaporation.[52−55] A pivotal aspect of **T**[**5**]'s versatility lies in its capacity to adapt its conformation and packing mode in response to the specific solvent employed in each experiment, as illustrated in Figure 2. Across various solvomorphs, **T**[**5**] undergoes conformational adjustments, leading to shifts in its overall shape and size, eventually enabling its molecular structure to optimize interactions with neighboring molecules. This property is particularly valuable in the domain of solid-state host−guest chemistry, where **T**[**5**] can function as a versatile host molecule, accommodating guests of diverse sizes and chemical properties. For instance, in the crystal structure of BZ@**T**[**5**], characterized by a 1:2 host−guest ratio, the BZ guests reside outside the **T**[**5**] cavity, as depicted in Figure 2a. On the other hand, the crystal structures

https://doi.org/10.1021/jacsau.4c00310
JACS Au 2024, 4, 3475−3483

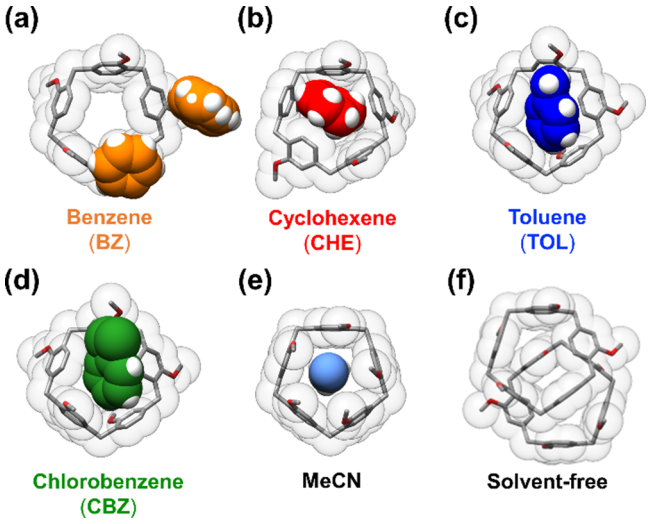

Figure 2. Host–guest arrangement and the altered conformations of **T**[5] as evidenced by single crystal structures. (a) BZ@**T**[5], (b) CHE@**T**[5], (c) TOL@**T**[5], (d) CBZ@**T**[5], (e) MeCN⊂**T**[5], and (f) solvent-free **T**[5] crystallized in $CHCl_3$, viewed from the top. Hydrogen atoms of the hosts are omitted for clarity. Color code: C, dark gray; O, red; N, light blue. Color code for guest molecules: BZ, orange; CHE, red; TOL, blue; CBZ, dark green.

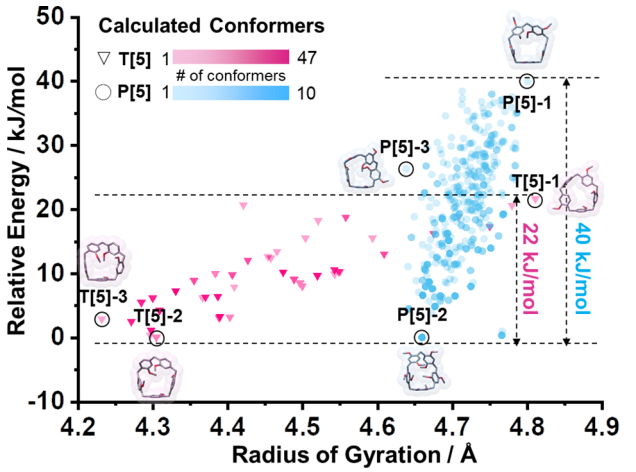

Figure 3. Conformational landscape of **T**[5] and **P**[5]. **T**[5] conformers are depicted by pink dots, while **P**[5] conformers are represented by blue dots. The landscape illustrates that **T**[5] conformers exhibit a wider distribution in both radius of gyration (R_g) and relative energy in comparison to **P**[5]. The calculated conformers with the highest and lowest relative energy for **T**[5] and **P**[5] are shown in black circle, respectively. **T**[5]-3 and **P**[5]-3 illustrate the conformers of **T**[5] and **P**[5] with the minimum radius of gyration.

of CHE@**T**[5], TOL@**T**[5], and CBZ@**T**[5] exhibit a 1:1 host–guest arrangement, where the guest molecules partially reside within the concave cavity of **T**[5] (Figure 2b–d). The primary driving forces behind the formation of these molecular assembles stem from the combination of multiple C–H···π and C–H···O interactions (Figures S1–S4). In stark contrast to these previously observed distorted conformations, a distinctly different structural arrangement emerged when **T**[5] was crystallized from acetonitrile (MeCN). In the MeCN@**T**[5] structure (Figure 2e),[50,56] all five aromatic units are aligned perpendicularly to the pentagonal aperture, forming a tiara-like shape to effectively host the guest molecule within. Another solvent-free **T**[5] crystal structure[50,57] is noteworthy for its tightly packed dimeric arrangement (Figure 2f). Intriguingly, two adjacent **T**[5] macrocycles each have one of their methoxy groups occupying the cavity of the other, indicating strong intermolecular interactions for dimeric arrangement. In light of these findings, it is evident that **T**[5] exhibits a diverse range of structural variations in the solid state.

2.2. Conformational Search Studies

In our pursuit of further understanding the conformational flexibility of the **T**[5] molecule, a thorough computational study involving conformational search was conducted,[58] commencing with the guest-free **T**[5] crystal structure. This extensive exploration yielded a total of 142 energy-accessible conformers (Figure 3, pink dots). For comparison, a similar conformational search was also conducted for the **P**[5] molecule, resulting in the identification of 423 energy-accessible conformers (Figure 3, blue dots). To ensure reliable optimized structures and accurate energy calculations, we employed density functional theory (DFT) calculations to determine the relative energies and optimized geometry of each conformer.[59] Notably, the energy gap between the highest and lowest energy conformers for **T**[5] was found to be 22 kJ/mol, indicative of a substantial degree of molecular flexibility. The presence of both compact and extended conformers in **T**[5] further underscores its conformational freedom.

To evaluate the conformational dynamics, flexibility, and rigidity of the macrocycle, we employed the radius of gyration (R_g). This parameter provides valuable insights into the spatial distribution of mass within the macrocyclic scaffold, hence serving as an indicator of its compactness or extension. The R_g values for the **T**[5] conformers exhibit a wider spread compared to those of the **P**[5] conformers, suggesting that **T**[5] possesses greater structural flexibility. The conformer with the highest relative energy exhibits five unfolded rims, resulting in a relatively extended and open conformation (**T**[5]-1 and **P**[5]-1; see Figure 3). Conversely, the conformer with the lowest relative energy or the minimum radius of gyration, characterized by the presence of five folded rims, respectively, adopts compact shapes (**T**[5]-2, **T**[5]-3, **P**[5]-2, and **P**[5]-3; see Figure 3).

Furthermore, we conducted a comprehensive investigation to determine the conformational properties of **T**[5] by utilizing a diverse set of initial conformers obtained from single cocrystal structures produced in various solvents. This analysis led to the identification of a cumulative count of 511 conformers, as depicted in Figure S5. Remarkably, regardless of the starting configuration employed for the conformational search, our findings consistently converged to the same conclusion.

In contrast, the energy difference between the highest and lowest energy conformers for **P**[5] was found to be 40 kJ/mol, suggesting a lower degree of flexibility compared to **T**[5]. The results of **P**[5] demonstrated a greater energy gap, indicative of a more restricted range of possible conformations. The **P**[5] conformer with the smallest radius or least relative energy display exhibits increased distortion and compactness compared to the conformer with the highest energy. These observations align with the experimental findings indicating that **T**[5] can readily switch between different conformers with low energy barriers when the crystallization conditions are altered.

https://doi.org/10.1021/jacsau.4c00310
JACS Au 2024, 4, 3475–3483

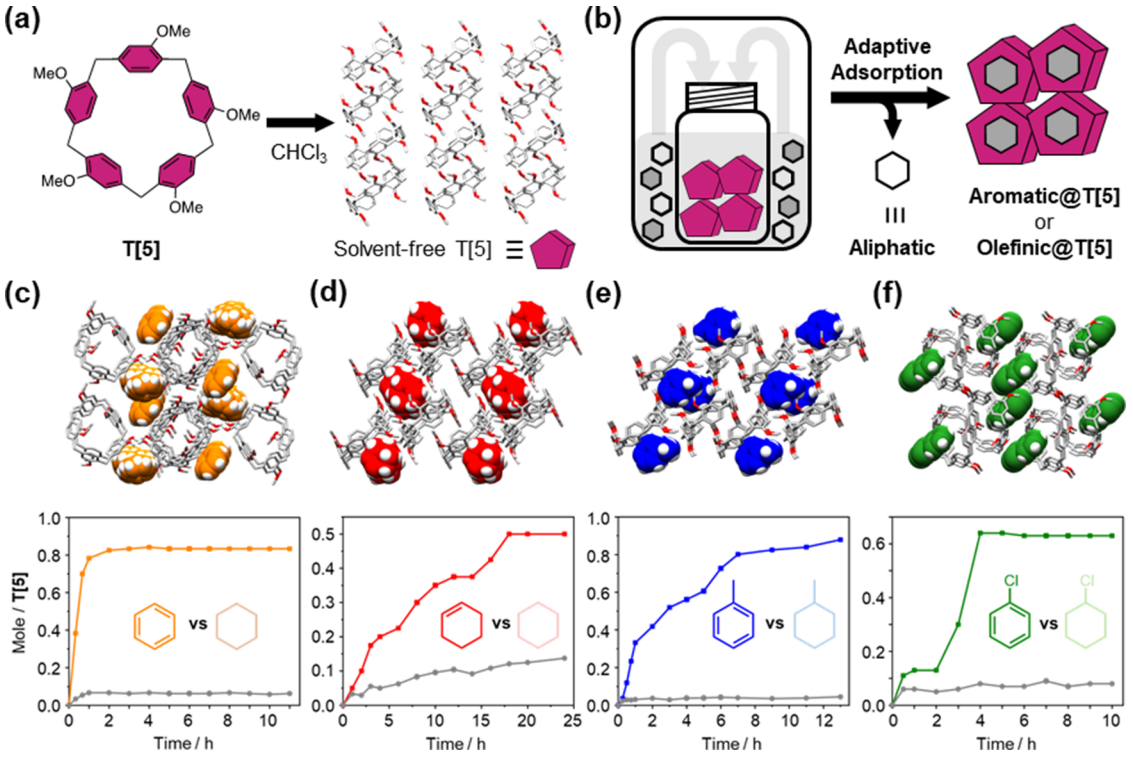

Figure 4. (a) Initial acquisition of solvent-free **T**[5] crystals via recrystallization in $CHCl_3$ solvent. (b) Schematic representation of the fractionation process for aromatic/olefinic compounds over aliphatics using **T**[5]-based nonporous adaptive crystals. (c–f) Single cocrystal structures of BZ@**T**[5], CHE@**T**[5], TOL@**T**[5], and CBZ@**T**[5], along with time-dependent vapor–solid sorption plots for (c) BZ/CH, (d) CHE/CH, (e) TOL/MCH, and (f) CBZ/CCH.

To ascertain the most optimized conformations from the pool of expected conformers, we employed a geometric matching approach, which involves comparing the gas-phase calculated conformations with structures obtained from single-crystal diffraction (Figure S6). The root-mean-square deviation (RMSD) value served as a metric to quantify geometric differences.[60] It was found that the calculated conformers exhibit geometric similarities to the conformations observed in the established phases of **T**[5] (see Figure S6). Nevertheless, notable differences, particularly in the orientation of the methoxy groups, were observed. This implies that molecules undergoing crystallization may not always be limited to adopting their lowest energy shape, and the conformations observed in experimental crystals may potentially influenced by kinetic factors.

Furthermore, we conducted geometric matching on single-crystal structures that underwent DFT optimization (Figure S7). Remarkably, it was observed that the single crystal structures exhibited a high level of concordance with the estimated structures following the optimization process, with a small RMSD value for each (Figure S7). ^{1}H NMR titration experiments were also conducted (Section 3 in SI, Figures S8–S11) to examine the flexibility between **T**[5] and **P**[5] in the solution state. All these identified conformational traits provide valuable insights into the inherent flexibility and adaptability of the **T**[5] macrocyclic scaffold.

The conformational study of **T**[5] and **P**[5] comprehensively demonstrated the remarkable conformational flexibility of the **T**[5] macrocycle through a series of detailed computational analyses. The investigation confirmed **T**[5]'s ability to access a wide array of conformers, significantly more diverse than **P**[5]. **T**[5] not only displayed a broad spectrum of structural variations, from compact to extended forms, but also adapted dynamically to varying conditions. Geometric matching approaches further underscored this adaptability, showing that **T**[5]'s crystalline forms might deviate from the lowest energy structures due to kinetic effects. This comprehensive collection of conformer data, coupled with geometric and energy assessments, firmly establish **T**[5] as a highly flexible and adaptable macrocyclic scaffold, well-suited for applications requiring molecular recognition and responsive adaptation to environmental fluctuations.

2.3. Solid–Vapor Sorption Experiments

To delve into the adsorption behavior of **T**[5] crystals, we conducted time-dependent solid–vapor sorption experiments. A guest-free **T**[5] crystalline material, obtained by slowly diffusing MeOH vapor into $CHCl_3$ solvent, was used as the adsorbent (Figure 4a). The absence of solvent molecules from the **T**[5] crystals was confirmed through ^{1}H NMR and thermogravimetric analysis (TGA) data, as shown in Figures S12 and S13, respectively. A bulk sample of desolvated **T**[5] was analyzed by powder X-ray diffraction (PXRD), confirming it to be both phase pure and representative of the single crystal data in its desolvated form (Figure S14). The N_2 adsorption isotherm at 77 K revealed the nonporous nature of this **T**[5] crystalline adsorbent, with a calculated Brunauer–Emmett–Teller (BET) surface area of merely 19 m^2/g (see Figure S15). Notwithstanding its initial nonporous nature, it is worth noting that similar pillararene macrocycles have been reported to exhibit adsorption performance due to structural changes induced by C–H···π interactions, aromatic π–π stacking, and charge-transfer interactions.[36,37]

https://doi.org/10.1021/jacsau.4c00310
JACS Au 2024, 4, 3475–3483

Time-dependent solid−vapor adsorption experiments were conducted to investigate the adsorption behaviors of various bicomponent aromatic/aliphatic or olefinic/aliphatic (50:50 *v*/*v*) vapors on the solvent-free **T[5]** crystalline material. The bicomponent atmospheres comprised four distinct combinations: benzene/cyclohexane (BZ/CH),[40,50,61−64] cyclohexene/cyclohexane (CHE/CH),[62] toluene/methylcyclohexane (TOL/MCH),[65] and chlorobenzene/chlorocyclohexane (CBZ/CCH).[66] In the BZ/CH atmosphere, ^{1}H NMR analysis indicated a gradual increase in BZ uptake by **T[5]**, reaching approximately 0.8 mol of BZ per **T[5]** after saturation (Figures 4c and S17). Conversely, only a minute amount of CH was adsorbed. Similarly, across the other bicomponent atmospheres, **T[5]** exhibited more effective adsorption of CHE, TOL, and CBZ compared to MCH, CCH, and CH, respectively. The ^{1}H NMR analysis revealed guest uptake of CBZ and TOL, with approximately 0.7−0.8 equiv molecules per **T[5]** after saturation. In contrast, CHE uptake was comparatively lower, as **T[5]** captured an average of about only 0.5 equiv of CHE from the equimolar CHE/CH mixture (shown in Figures 4d−f and S18−S20).

Solid-state packings of single crystal structures of BZ@**T[5]**, CHE@**T[5]**, TOL@**T[5]**, and CBZ@**T[5]** are shown in Figure 4c−f. In these superstructures, solvent guests are located in the extrinsic cavity. Hirshfeld surface analysis was employed to investigate the intermolecular interactions present in these cocrystal structures. In the context of BZ@**T[5]**, CBZ@**T[5]**, and TOL@**T[5]** inclusion, we observed the presence of C−H···O interactions between the host molecules, as well as between the host and guest molecules (refer to Figures S21−S23). Nevertheless, inside the CHE@**T[5]** inclusion compound, our observations were limited to C−H···O interactions only among the host molecules (Figure S24). It is conceivable that **T[5]** has a greater propensity to acquire BZ, CBZ, and TOL compared to CHE. According to the examination of the Hirshfeld surface, it can be inferred that the adsorption capacity of **T[5]** for CHE is comparatively lower, possibly due to the lack of C−H···O interactions between CHE and **T[5]**. These findings shed light on the precise interactions governing the adsorption behavior of **T[5]** with various guests, thereby enhancing our understanding of its separation capacities.

To access the structural changes induced by the encapsulation of guest molecules within **T[5]**, we carried out PXRD studies following the adsorption of pure BZ, CHE, CBZ, and TOL by **T[5]**, respectively. Notably, the PXRD patterns of **T[5]** underwent pronounced alterations after the adsorption of these solvents. These patterns correlated with the simulated PXRD profiles generated from the single crystal structures of BZ@**T[5]**, CHE@**T[5]**, TOL@**T[5]**, and CBZ@**T[5]**. However, clear deviations were observed between the post-adsorption PXRD patterns and their respective single-crystal structure patterns. These discrepancies might arise from factors such as surface adsorption effects and variations in the quantity of guest molecules entrapped within **T[5]** (Figure S25). On the other hand, the PXRD patterns of **T[5]** remained unaltered following the adsorption of CH, MCH, and CCH, suggesting that the structural integrity of **T[5]** was unaffected by its exposure to these solvents (Figures S26−S29). We also validated the guest uptakes by gas chromatography (GC) and TGA analysis. GC results confirmed the predominant uptake of aromatic or olefinic compounds compared to aliphatic ones in **T[5]** (Figure S30). Furthermore, TGA analysis revealed a weight loss attributed to the release of the adsorbed guest molecules from **T[5]**, providing additional evidence of successful adsorption and storage of the aromatic/olefinic compounds (Figure S31). For separation materials of this nature, a notable challenge arises from the decrease in performance after multiple uses, potentially stemming from issues like fouling, structural alterations, and material degradation. Therefore, the ability to restore utility and sustain stability over numerous adsorption and desorption cycles becomes imperative. In our investigation, we noted a noteworthy phenomenon: the adsorbed aromatic molecules can be liberated when subjected to heat. This property enables **T[5]** to undergo reactivation, rendering it suitable for repeated cycles of adsorption (Figures S32−S35). This adaptability and reusability of nonporous **T[5]** crystalline materials represent a remarkable advantage for adsorbent cycles.

2.4. Rationalizing Adsorption Selectivity

Upon examining various adsorption conditions of **T[5]** crystals, a clear preference becomes evident: **T[5]** exhibits a propensity for encapsulating aromatic/olefinic solvents over their aliphatic counterparts. To elucidate the underlying molecular interplays, we turned to molecular docking. This approach, outlined in Figure 5a, aimed to generate host−guest

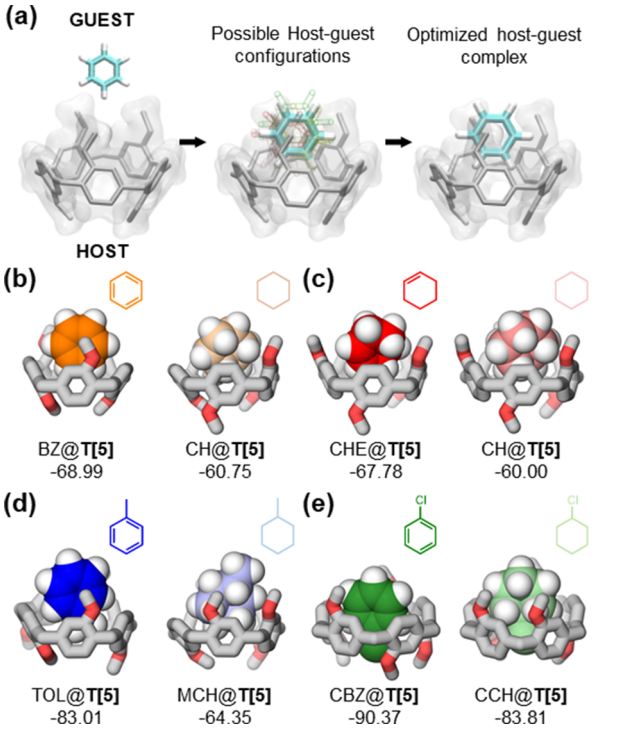

Figure 5. (a) Simplified docking process overview. *Left*: input structures of individual host and guest molecules. *Center*: molecular docking procedures involving the search for the optimal host−guest binding mode, including randomly sampled poses through translation, rotational, and torsional operations. The faded benzenes represent trial poses, while the solid cyan benzene represents the stable pose. *Right*: The docking results. (b-e) Geometry-optimized 1:1 host−guest structures obtained from molecular docking were subsequently used for binding energy calculations. The host molecules are shown in gray, while the guest molecules for (b) BZ/CH molecules are shown in orange and wheat, (c) CHE/CH in red and salmon, (d) TOL/MCH molecule in blue and light blue, and (e) CBZ/CCH in dark green and pale green. The unit of binding energy is measured in kJ/mol.

https://doi.org/10.1021/jacsau.4c00310
JACS Au 2024, 4, 3475−3483

complexes of both aromatic/olefinic@**T**[5] and aliphatic@**T**[5]. This docking analysis was performed using Glide as implemented in Schrodinger.[67] Molecular docking serves as a predictive tool, providing insights into how two molecules might orient themselves to form a stable complex with optimal binding.[68] This approach allowed us to pinpoint the most favorable low-energy structures for both the aromatic/olefinic@**T**[5] and aliphatic@**T**[5] host−guest pairs. Building on this, we performed DFT-D geometry optimization of these complexes, utilizing the results from the docking study as our starting point.[69] The geometry optimized conformations of aromatic/olefinic@**T**[5] and aliphatic@**T**[5] complexes are shown in Figure 5b−e.

Upon closer examination of the binding energy analysis, a consistent trend emerged: the aromatic/olefinic@**T**[5] complexes consistently register lower binding energies in contrast to their aliphatic@**T**[5] counterparts. In the case of the aromatic/olefinic complexes, noticeable discrepancies between the docking predictions and the actual crystal structures were observed, possibly stemming from the absence of certain intermolecular forces during the stacking phase (as illustrated in Figure S36a−h). While numerous factors can influence the binding energy in supramolecular host−guest systems, our calculations suggest that the $\pi-\pi$ interactions observed between **T**[5]'s arenes and aromatic guest molecules in the optimized geometries could be the driving force behind their energetically favorable nature, especially when compared to aliphatic molecules (refer to Figures S36i,k,l and S37). Even though the derived docking models may deviate from the actual crystal forms, they shed light on the molecular intricacies influencing adsorption selectivity. All evidence points to **T**[5] showcasing an innate preference for cocrystallization with aromatic/olefinic solvents, leading to the formation of more robust host−guest assemblages than with aliphatic counterparts.

3. CONCLUSIONS

In summary, our study has offered a comprehensive insight into the conformational versatility displayed by **T**[5] through a variety of analytical approaches. X-ray crystallography analysis has revealed the presence of multifaceted conformations of **T**[5] in the solid state, shedding light on its structural adaptability. Our theoretical exploration of conformational energy landscapes has allowed us to pinpoint stable **T**[5] conformers and emphasize the minor energy differential (22 kJ/mol) between the highest and lowest energy states, underscoring its flexible nature. Furthermore, our solid−vapor sorption experiments have unveiled a significant revelation: **T**[5] initially exhibits nonporosity in its guest-free state, undergoes a transformative shift when introduced to aromatic/olefinic vapors, underscoring its pronounced predilection for these specific guest entities. Insights from single-crystal analyses, X-ray diffraction, and molecular simulation converge to suggest that this selectivity arises from guest-induced structural alterations. Such sorption behavior diverges from traditional adsorptive processes which utilize materials with pre-existing pores. For **T**[5]-based crystalline materials, the formation of these "pores" takes place during crystalline inclusion compound assembly and typically maintains stability when filled by guest entities.

These findings underscore the adeptness of **T**[5] in discerningly separating aromatic/olefinic solvents from balanced mixtures with analogous aliphatics. Considering its high conformational flexibility, exceptional performance in separation capabilities, and excellent reusability, **T**[5]-based crystal emerges as a promising contender for tackling intricate challenges related to molecular separation. These findings provide valuable insight into the design and synthesis of macrocycle-based crystalline materials, offering sustainable and efficient solutions for various industrial processes.

4. METHODS

4.1. Materials and General Experimental Methods

Starting materials, reagents, and solvents were purchased from commercial vendors and used as received, unless otherwise noted. Permethylated tiara[5]arene (**T**[5]) was synthesized by a synthetic procedure previously reported.[49] ^{1}H NMR spectra were recorded on Bruker Advance 400 and 600 MHz spectrometer at ambient temperature, unless otherwise noted. The chemical shifts are listed in ppm on the δ scale and coupling constants were recorded in Hz. Chemical shifts are calibrated relative to the signals of the nondeuterated solvents ($CHCl_3$: δ 7.26 ppm, CH_2Cl_2: δ 5.32 ppm). Thermogravimetric analysis (TGA) was performed with METTLER TOLEDO TGA 2 operated at 10 K·min^{-1}. Powder X-ray diffraction (PXRD) patterns were recorded on a Rigaku D/Max-2500 X-ray diffractometer. Data were collected over the range of 3−40° in 5°·min^{-1}. N_2 adsorption measurements were carried out on a Micromeritics ASAP 2020 gas adsorption analyzer at 77 K before **T**[5] was heated at 60 °C in vacuo for 12 h. Gas chromatography (GC) measurements were carried out on a Shimadzu GCMS-QP2010 Plus with an FID detector. Samples were analyzed using headspace injections and were performed by incubating the sample at 50 °C for 5 min followed by sampling 1 mL of the headspace.

4.2. Single Crystal X-ray Diffraction

Colorless block crystals of different **T**[5] solvomorphs were grown by slow evaporation of the corresponding solutions of **T**[5] (solvent: benzene (BZ)/cyclohexane (CHE)/toluene (TOL)/chlorobenzene (CBZ), 1 mL; **T**[5], 5 mg). After several days, single crystals suitable for X-ray diffraction were selected and mounted in inert oil in cold gas stream and their X-ray diffraction intensity data was collected on a Rigaku XtaLAB FRX diffractometer equipped with a Hypix6000HE detector, using Cu $K\alpha$ radiation (λ = 1.54184 Å). Crystals were kept at the temperature listed in Tables S1−S3 during data collection. By the use of Olex2,[70] the structure was solved either (i) with the ShelXS[71] structure solution program using Direct Methods or (ii) with the ShelXT[72] structure solution program using Direct Methods or Intrinsic Phasing. The hydrogen atoms were set in calculated positions and refined as riding atoms with a common fixed isotropic thermal parameter. Selected details of the data collection and structural refinement can be found within Tables S1−S3 and full details are available in the corresponding CIF files. The crystal structures of BZ@**T**[5] and solvent-free **T**[5] were previously reported.[50]

4.3. Conformer Search

The initial conformers are derived from the guest-free single crystals of both **P**[5] and **T**[5]. Additionally, a more detailed conformer search uses the single crystal structures of various solvents. Upon obtaining the conformers, the structure is optimized using the OPLS3e force field,[73] as incorporated in Schrödinger.[74] Minimum and maximum distance for LMOD[75] of 6 and 12 Å are applied and 3000 search steps are used. When preserving structures, an energy window is set to within 50 kJ/mol, and a 1 Å cutoff is established for maximum atomic deviation, accounting for potential force field inaccuracies. While it is widely recognized that solely using a force field for molecule optimization can be unreliable,[59] even though OPLS3e has demonstrated effectiveness in organic systems. Consequently, structures derived from the conformer search are further optimized at the DFT-D level using B3LYP[69,76] function with 6-311G* basis sets, and Grimme's D3 scheme with Becke and Johnson damping,[77,78] all executed in Gaussian 09.[79]

https://doi.org/10.1021/jacsau.4c00310
JACS Au 2024, 4, 3475−3483

4.4. Binding Energy Calculation

The binding energy,[80] denoted as $\Delta E_{\text{binding energy}}$, is calculated based on the energy difference between the host−guest complex and the summed energies of the independent host and guest molecules, each in its energy-minimized conformation. The equation can be found in the Supporting Information.

The structures of aromatic@**T**[**5**], olefinic@**T**[**5**], and aliphatic@**T**[**5**] complexes are intricate. These complexes were generated using the Glide module[67] of Schrödinger V13.2 to obtain their docking configurations. All employed force field parameters are based on the OPLS4[81] framework within Schrödinger. For the LigPrep stage, ionization states remain unchanged, and the specified chirality is maintained. A maximum of 32 stereoisomers per ligand is generated. The Protein Preparation Workflow uses default settings for each **T**[**5**] host molecule. During the receptor grid generation, the van der Waals radius scaling factor is set to 1.0, with a partial charge cutoff of 0.25. For Ligand Docking, these values are adjusted to 0.8 and 0.15, respectively. The precision method is standard precision, and ligand sampling is set to flexible, incorporating both nitrogen inversions and ring conformation sampling.

All DFT calculations were performed in Gaussian09,[79] aiming to identify the absolute minimum conformation. The DFT-D geometry optimization employs the B3LYP functional with a 6-311G* basis set.[69,76] Additionally, dispersion energy corrections are Grimme's D3 scheme with Becke and Johnson (BJ) damping.[77,78]

■ ASSOCIATED CONTENT

Supporting Information

The Supporting Information is available free of charge at https://pubs.acs.org/doi/10.1021/jacsau.4c00310.

X-ray crystallography, conformer search, host−guest binding studies in solution, vapor−solid fractionation experiments, binding energy and cavity size calculations (PDF)

■ AUTHOR INFORMATION

Corresponding Authors

Shan Jiang − *School of Physical Science and Technology, ShanghaiTech University, Shanghai 201210, China*; Email: jiangshan@shanghaitech.edu.cn

Andrew C.-H. Sue − *College of Chemistry and Chemical Engineering, Xiamen University, Xiamen 361005, China*; orcid.org/0000-0001-9557-2658; Email: andrewsue@xmu.edu.cn

Authors

Zezhao Xu − *School of Physical Science and Technology, ShanghaiTech University, Shanghai 201210, China*; orcid.org/0009-0004-0928-9573

Weiwei Yang − *Institute for Molecular Design and Synthesis, Tianjin University, Tianjin 300072, China*; orcid.org/0000-0003-3062-6023

Huiyu Liu − *School of Physical Science and Technology, ShanghaiTech University, Shanghai 201210, China*

Complete contact information is available at: https://pubs.acs.org/10.1021/jacsau.4c00310

Author Contributions

[‖]Z.X. and W.Y. are co-first authors. These authors contributed equally. The manuscript was written through the contributions of all authors. All authors have given approval to the final version of the manuscript. A.C.-H.S. and S.J. conceived the idea and supervised the project. Z.X. designed the computational part and carried out the conformational search, binding energy calculation, Hirshfeld Surface analysis, and wrote the manuscript. W.Y. designed the experimental part, carried out the ^{1}H NMR, X-ray diffraction, and solid−vapor sorption, and wrote the original draft. H.L. contributed to the manuscript writing.

Notes

The authors declare no competing financial interest.

■ ACKNOWLEDGMENTS

This work received support from various funding sources, including ShanghaiTech University Startup Fund, the Science and Technology Commission of Shanghai Municipality (21JC1401700), Shanghai Pujiang Program, and Shanghai Synchrotron Radiation Facility, instrument at Beamline BL14B1, Beamline BL17B and Beamline BL10U2 (proposal 2022-SSRF-PT-501031 and 2022-SSRF-PT-021501). S.J., H.L., and A.C.-H.S. gratefully acknowledge financial support from the National Natural Science Foundation of China (22001169, 22205143, 22371241). H.L. also acknowledges funding from the China Postdoctoral Science Foundation (2022M712137), and the Shanghai Postdoctoral Excellence Program. A.C.-H.S. expresses appreciation for the support received from the Starry Night Science Fund of Zhejiang University's Shanghai Institute for Advanced Study (SN-ZJU-SIAS-006).

■ DEDICATION

[⊥]We dedicate this paper to the late Prof. Wei Jiang of SUSTech University.

■ REFERENCES

(1) Lehn, J.-M. Supramolecular Chemistry—Scope and Perspectives Molecules, Supermolecules, and Molecular Devices (Nobel Lecture). *Angew. Chem., Int. Ed. Engl.* **1988**, *27* (1), 89−112.

(2) Steed, J. W.; Atwood, J. L. *Supramolecular Chemistry*; John Wiley & Sons, Inc.: Chichester, 2022.

(3) Harada, A.; Hashidzume, A.; Yamaguchi, H.; Takashima, Y. Polymeric Rotaxanes. *Chem. Rev.* **2009**, *109* (11), 5974−6023.

(4) Aida, T.; Meijer, E. W.; Stupp, S. I. Functional Supramolecular Polymers. *Science* **2012**, *335* (6070), 813−817.

(5) Liu, K.; Kang, Y.; Wang, Z.; Zhang, X. 25th Anniversary Article: Reversible and Adaptive Functional Supramolecular Materials: "Noncovalent Interaction" Matters. *Adv. Mater.* **2013**, *25* (39), 5530−5548.

(6) Amabilino, D. B.; Smith, D. K.; Steed, J. W. Supramolecular Materials. *Chem. Soc. Rev.* **2017**, *46* (9), 2404−2420.

(7) Yamamoto, Y.; Fukushima, T.; Suna, Y.; Ishii, N.; Saeki, A.; Seki, S.; Tagawa, S.; Taniguchi, M.; Kawai, T.; Aida, T. Photoconductive Coaxial Nanotubes of Molecularly Connected Electron Donor and Acceptor Layers. *Science* **2006**, *314* (5806), 1761−1764.

(8) Davis, J. T.; Gale, P. A.; Quesada, R. Advances in Anion Transport and Supramolecular Medicinal Chemistry. *Chem. Soc. Rev.* **2020**, *49* (16), 6056−6086.

(9) Williams, G. T.; Haynes, C. J. E.; Fares, M.; Caltagirone, C.; Hiscock, J. R.; Gale, P. A. Advances in Applied Supramolecular Technologies. *Chem. Soc. Rev.* **2021**, *50* (4), 2737−2763.

(10) Tang, M.; Zhong, Z.; Ke, C. Advanced Supramolecular Design for Direct Ink Writing of Soft Materials. *Chem. Soc. Rev.* **2023**, *52* (5), 1614−1649.

(11) Zhang, G.; Emwas, A.-H.; Shahul Hameed, U. F.; Arold, S. T.; Yang, P.; Chen, A.; Xiang, J.-F.; Khashab, N. M. Shape-Induced Selective Separation of *ortho*-Substituted Benzene Isomers Enabled by Cucurbit[7]uril Host Macrocycles. *Chem.* **2020**, *6* (5), 1082−1096.

(12) Xia, D.; Wang, P.; Ji, X.; Khashab, N. M.; Sessler, J. L.; Huang, F. Functional Supramolecular Polymeric Networks: The Marriage of Covalent Polymers and Macrocycle-Based Host−Guest Interactions. *Chem. Rev.* **2020**, *120* (13), 6070−6123.
(13) Skorjanc, T.; Shetty, D.; Trabolsi, A. Pollutant Removal with Organic Macrocycle-Based Covalent Organic Polymers and Frameworks. *Chem.* **2021**, *7* (4), 882−918.
(14) Zhang, G.; Lin, W.; Huang, F.; Sessler, J.; Khashab, N. M. Industrial Separation Challenges: How Does Supramolecular Chemistry Help? *J. Am. Chem. Soc.* **2023**, *145* (35), 19143−19163.
(15) Zhu, H.; Chen, L.; Sun, B.; Wang, M.; Li, H.; Stoddart, J. F.; Huang, F. Applications of Macrocycle-Based Solid-State Host−Guest Chemistry. *Nat. Rev. Chem.* **2023**, *7*, 768−782.
(16) Li, Q.; Zhang, W.; Miljanić, O. Š.; Sue, C.-H.; Zhao, Y.-L.; Liu, L.; Knobler, C. B.; Stoddart, J. F.; Yaghi, O. M. Docking in Metal-Organic Frameworks. *Science* **2009**, *325* (5942), 855−859.
(17) Strutt, N. L.; Fairen-Jimenez, D.; Iehl, J.; Lalonde, M. B.; Snurr, R. Q.; Farha, O. K.; Hupp, J. T.; Stoddart, J. F. Incorporation of an A1/A2-Difunctionalized Pillar[5]arene into a Metal−Organic Framework. *J. Am. Chem. Soc.* **2012**, *134* (42), 17436−17439.
(18) Zhang, K.-D.; Tian, J.; Hanifi, D.; Zhang, Y.; Sue, A. C.-H.; Zhou, T.-Y.; Zhang, L.; Zhao, X.; Liu, Y.; Li, Z.-T. Toward a Single-Layer Two-Dimensional Honeycomb Supramolecular Organic Framework in Water. *J. Am. Chem. Soc.* **2013**, *135* (47), 17913−17918.
(19) Zhang, H.; Zou, R.; Zhao, Y. Macrocycle-Based Metal-Organic Frameworks. *Coord. Chem. Rev.* **2015**, *292*, 74−90.
(20) Yuan, Y.; Bang, K.-T.; Wang, R.; Kim, Y. Macrocycle-Based Covalent Organic Frameworks. *Adv. Mater.* **2023**, *35* (16), No. 2210952.
(21) Barbour, L. J. Crystal Porosity and the Burden of Proof. *Chem. Commun.* **2006**, *11*, 1163−1168.
(22) Atwood, J. L.; Barbour, L. J.; Jerga, A.; Schottel, B. L. Guest Transport in a Nonporous Organic Solid via Dynamic van der Waals Cooperativity. *Science* **2002**, *298* (5595), 1000−1002.
(23) Dalgarno, S. J.; Thallapally, P. K.; Barbour, L. J.; Atwood, J. L. Engineering Void Space in Organic van der Waals Vrystals: Calixarenes Lead the Way. *Chem. Soc. Rev.* **2007**, *36* (2), 236−245.
(24) Ogoshi, T.; Kanai, S.; Fujinami, S.; Yamagishi, T.-A.; Nakamoto, Y. *para*-Bridged Symmetrical Pillar[5]arenes: Their Lewis Acid Catalyzed Synthesis and Host−Guest Property. *J. Am. Chem. Soc.* **2008**, *130* (15), 5022−5023.
(25) Cao, D.; Kou, Y.; Liang, J.; Chen, Z.; Wang, L.; Meier, H. A Facile and Efficient Preparation of Pillararenes and a Pillarquinone. *Angew. Chem., Int. Ed.* **2009**, *48* (51), 9721−9723.
(26) Strutt, N. L.; Zhang, H.; Schneebeli, S. T.; Stoddart, J. F. Functionalizing Pillar[*n*]arenes. *Acc. Chem. Res.* **2014**, *47* (8), 2631−2642.
(27) Ogoshi, T.; Yamagishi, T.-A.; Nakamoto, Y. Pillar-Shaped Macrocyclic Hosts Pillar[*n*]arenes: New Key Players for Supramolecular Chemistry. *Chem. Rev.* **2016**, *116* (14), 7937−8002.
(28) Ogoshi, T.; Kakuta, T.; Yamagishi, T.-A. Applications of Pillar[*n*]arene-Based Supramolecular Assemblies. *Angew. Chem., Int. Ed.* **2019**, *58* (8), 2197−2206.
(29) Song, N.; Kakuta, T.; Yamagishi, T.-A.; Yang, Y.-W.; Ogoshi, T. Molecular-Scale Porous Materials Based on Pillar[*n*]arenes. *Chem* **2018**, *4* (9), 2029−2053.
(30) Zhou, Y.; Jie, K.; Zhao, R.; Huang, F. Supramolecular-Macrocycle-Based Crystalline Organic Materials. *Adv. Mater.* **2020**, *32* (20), No. 1904824.
(31) Wu, J.-R.; Yang, Y.-W. Synthetic Macrocycle-Based Nonporous Adaptive Crystals for Molecular Separation. *Angew. Chem., Int. Ed.* **2021**, *60* (4), 1690−1701.
(32) Ohtani, S.; Kato, K.; Fa, S.; Ogoshi, T. Host−Guest Chemistry Based on Solid-State Pillar[*n*]arenes. *Coord. Chem. Rev.* **2022**, *462*, No. 214503.
(33) Tan, L.-L.; Li, H.; Tao, Y.; Zhang, S. X.-A.; Wang, B.; Yang, Y.-W. Pillar[5]arene-Based Supramolecular Organic Frameworks for Highly Selective CO_2-Capture at Ambient Conditions. *Adv. Mater.* **2014**, *26* (41), 7027−7031.
(34) Ogoshi, T.; Sueto, R.; Yoshikoshi, K.; Yamagishi, T.-A. One-Dimensional Channels Constructed from Per-Hydroxylated pillar[6]arene Molecules for Gas and Vapour Adsorption. *Chem. Commun.* **2014**, *50* (96), 15209−15211.
(35) Tan, L.-L.; Zhu, Y.; Long, H.; Jin, Y.; Zhang, W.; Yang, Y.-W. Pillar[*n*]arene-based Supramolecular Organic Frameworks with High Hydrocarbon Storage and Selectivity. *Chem. Commun.* **2017**, *53* (48), 6409−6412.
(36) Jie, K.; Zhou, Y.; Li, E.; Huang, F. Nonporous Adaptive Crystals of Pillararenes. *Acc. Chem. Res.* **2018**, *51* (9), 2064−2072.
(37) Yan, M.; Wang, Y.; Chen, J.; Zhou, J. Potential of Nonporous Adaptive Crystals for Hydrocarbon Separation. *Chem. Soc. Rev.* **2023**, *52* (17), 6075−6119.
(38) Jie, K.; Liu, M.; Zhou, Y.; Little, M. A.; Bonakala, S.; Chong, S. Y.; Stephenson, A.; Chen, L.; Huang, F.; Cooper, A. I. Styrene Purification by Guest-Induced Restructuring of Pillar[6]arene. *J. Am. Chem. Soc.* **2017**, *139* (8), 2908−2911.
(39) Jie, K.; Liu, M.; Zhou, Y.; Little, M. A.; Pulido, A.; Chong, S. Y.; Stephenson, A.; Hughes, A. R.; Sakakibara, F.; Ogoshi, T.; et al. Near-Ideal Xylene Selectivity in Adaptive Molecular Pillar[*n*]arene Crystals. *J. Am. Chem. Soc.* **2018**, *140* (22), 6921−6930.
(40) Moosa, B.; Alimi, L. O.; Lin, W.; Fakim, A.; Bhatt, P. M.; Eddaoudi, M.; Khashab, N. M. Fluorine-Boosted Kinetic and Selective Molecular Sieving of C6 Derivatives. *Angew. Chem., Int. Ed.* **2023**, *62*, No. e202311555.
(41) Ogoshi, T.; Sueto, R.; Yoshikoshi, K.; Sakata, Y.; Akine, S.; Yamagishi, T.-A. Host−Guest Complexation of Perethylated Pillar[5]arene with Alkanes in the Crystal State. *Angew. Chem., Int. Ed.* **2015**, *54* (34), 9849−9852.
(42) Ogoshi, T.; Shimada, Y.; Sakata, Y.; Akine, S.; Yamagishi, T.-A. Alkane-Shape-Selective Vapochromic Behavior Based on Crystal-State Host−Guest Complexation of Pillar[5]arene Containing One Benzoquinone Unit. *J. Am. Chem. Soc.* **2017**, *139* (16), 5664−5667.
(43) Ogoshi, T.; Saito, K.; Sueto, R.; Kojima, R.; Hamada, Y.; Akine, S.; Moeljadi, A. M. P.; Hirao, H.; Kakuta, T.; Yamagishi, T.-A. Separation of Linear and Branched Alkanes Using Host−Guest Complexation of Cyclic and Branched Alkane Vapors by Crystal State Pillar[6]arene. *Angew. Chem., Int. Ed.* **2018**, *57* (6), 1592−1595.
(44) Jie, K.; Zhou, Y.; Li, E.; Zhao, R.; Liu, M.; Huang, F. Linear Positional Isomer Sorting in Nonporous Adaptive Crystals of a Pillar[5]arene. *J. Am. Chem. Soc.* **2018**, *140* (9), 3190−3193.
(45) Wu, J.-R.; Li, B.; Yang, Y.-W. Separation of Bromoalkanes Isomers by Nonporous Adaptive Crystals of Leaning Pillar[6]arene. *Angew. Chem., Int. Ed.* **2020**, *59* (6), 2251−2255.
(46) Ogoshi, T.; Kitajima, K.; Aoki, T.; Fujinami, S.; Yamagishi, T.-A.; Nakamoto, Y. Synthesis and Conformational Characteristics of Alkyl-Substituted Pillar[5]arenes. *J. Org. Chem.* **2010**, *75* (10), 3268−3273.
(47) Du, K.; Demay-Drouhard, P.; Samanta, K.; Li, S.; Thikekar, T. U.; Wang, H.; Guo, M.; van Lagen, B.; Zuilhof, H.; Sue, A. C.-H. Stereochemical Inversion of Rim-Differentiated Pillar[5]arene Molecular Swings. *J. Org. Chem.* **2020**, *85* (17), 11368−11374.
(48) Guo, M.; Wang, X.; Zhan, C.; Demay-Drouhard, P.; Li, W.; Du, K.; Olson, M. A.; Zuilhof, H.; Sue, A. C.-H. Rim-Differentiated C_5-Symmetric Tiara-Pillar[5]arenes. *J. Am. Chem. Soc.* **2018**, *140* (1), 74−77.
(49) Demay-Drouhard, P.; Du, K.; Samanta, K.; Wan, X.; Yang, W.; Srinivasan, R.; Sue, A. C.-H.; Zuilhof, H. Functionalization at Will of Rim-Differentiated Pillar[5]arenes. *Org. Lett.* **2019**, *21* (11), 3976−3980.
(50) Yang, W.; Samanta, K.; Wan, X.; Thikekar, T. U.; Chao, Y.; Li, S.; Du, K.; Xu, J.; Gao, Y.; Zuilhof, H.; et al. Tiara[5]arenes: Synthesis, Solid-State Conformational Studies, Host−Guest Properties, and Application as Nonporous Adaptive Crystals. *Angew. Chem., Int. Ed.* **2020**, *59* (10), 3994−3999.
(51) Liu, P.; Li, Q.; Zeng, H.; Shi, B.; Liu, J.; Huang, F. [1_5]Paracyclophane and [1_6]paracyclophane: Facile Syntheses, Crystal Structures and Selective Complexation with Cesium Cations in the Gas Phase. *Org. Chem. Front.* **2019**, *6* (3), 309−312.

https://doi.org/10.1021/jacsau.4c00310
JACS Au 2024, 4, 3475−3483

(52) Crystallographic data for BZ@**T**[**5**] was previously reported.[50] CCDC 1957867.
(53) Crystallographic data for CHE@**T**[**5**]: $C_{46}H_{50}O_5$; triclinic, space group $P\bar{1}$; a = 11.2771(2), b = 12.8743(2), c = 14.6800(2) Å; α = 98.3870(10), β = 101.7480(10), γ = 112.1970(10)°; V = 1872.77(5) Å^3; Z = 2; ρ_{calc} = 1.211 gcm^{-3}; $2\theta_{max}$ = 149.586; T = 159.99 K; 21,076 reflections collected, 7383 independent, 465 parameters; μ = 0.607 mm^{-1}; R_1 = 0.0458 [$I > = 2\sigma(I)$], wR_2 = 0.1301 (all data). CCDC 2292521.
(54) Crystallographic data for TOL@**T**[**5**]: $C_{47}H_{48}O_5$; triclinic, space group $P\bar{1}$; a = 11.1541(2), b = 12.8664(3), c = 12.8664(3) Å; α = 93.752(2), β = 107.106(2), γ = 111.782(2)°; V = 1879.47(7) Å^3; Z = 2; ρ_{calc} = 1.224 gcm^{-3}; $2\theta_{max}$ = 149.172; T = 160.00 K; 23,256 reflections collected, 7298 independent, 475 parameters; μ = 0.615 mm^{-1}; R_1 = 0.0478 [$I > = 2\sigma(I)$], wR_2 = 0.1246 (all data). CCDC 2292522.
(55) Crystallographic data for CBZ@**T**[**5**]: $C_{46}H_{45}ClO_5$; triclinic, space group $P\bar{1}$; a = 11.1195(10), b = 12.8431(2), c = 15.0766(2) Å; α = 93.6320(10), β = 107.4120(10), γ = 111.5760(10) °; V = 1873.63(4) Å^3; Z = 2; ρ_{calc} = 1.264 gcm^{-3}; $2\theta_{max}$ = 148.864; T = 159.99 K; 53,825 reflections collected, 7319 independent, 484 parameters; μ = 1.273 mm^{-1}; R_1 = 0.0532 [$I > = 2\sigma(I)$], wR_2 = 0.1431 (all data). CCDC 2292520.
(56) Crystallographic data for MeCN⊂**T**[**5**] was previously reported. [50]CCDC 1896025.
(57) Crystallographic data for solvent-free **T**[**5**] was previously reported. [50]CCDC 1957868.
(58) Mohamadi, F.; Richards, N. G. J.; Guida, W. C.; Liskamp, R.; Lipton, M.; Caufield, C.; Chang, G.; Hendrickson, T.; Still, W. C. Macromodel—An Integrated Software System for Modeling Organic and Bioorganic Molecules Using Molecular Mechanics. *J. Comput. Chem.* **1990**, *11* (4), 440−467.
(59) Thompson, H. P. G.; Day, G. M. Which Conformations Make Stable Crystal Structures? Mapping Crystalline Molecular Geometries to the Conformational Energy Landscape. *Chem. Sci.* **2014**, *5* (8), 3173−3182.
(60) Carugo, O. How Root-Mean-Square Distance (r.m.s.d.) Values Depend on the Resolution of Protein Structures that are Compared. *J. Appl. Crystallogr.* **2003**, *36* (1), 125−128.
(61) Zhou, J.; Yu, G.; Li, Q.; Wang, M.; Huang, F. Separation of Benzene and Cyclohexane by Nonporous Adaptive Crystals of a Hybrid[3]arene. *J. Am. Chem. Soc.* **2020**, *142* (5), 2228−2232.
(62) Yao, H.; Wang, Y.-M.; Quan, M.; Farooq, M. U.; Yang, L.-P.; Jiang, W. Adsorptive Separation of Benzene, Cyclohexene, and Cyclohexane by Amorphous Nonporous Amide Naphthotube Solids. *Angew. Chem., Int. Ed.* **2020**, *59* (45), 19945−19950.
(63) Ding, Y.; Alimi, L. O.; Moosa, B.; Maaliki, C.; Jacquemin, J.; Huang, F.; Khashab, N. M. Selective Adsorptive Separation of Cyclohexane over Benzene Using Thienothiophene Cages. *Chem. Sci.* **2021**, *12* (14), 5315−5318.
(64) Cui, P.-F.; Liu, X.-R.; Lin, Y.-J.; Li, Z.-H.; Jin, G.-X. Highly Selective Separation of Benzene and Cyclohexane in a Spatially Confined Carborane Metallacage. *J. Am. Chem. Soc.* **2022**, *144* (14), 6558−6565.
(65) Jie, K.; Zhou, Y.; Li, E.; Zhao, R.; Huang, F. Separation of Aromatics/Cyclic Aliphatics by Nonporous Adaptive Pillararene Crystals. *Angew. Chem., Int. Ed.* **2018**, *57* (39), 12845−12849.
(66) Wu, J.-R.; Yang, Y.-W. Geminiarene: Molecular Scale Dual Selectivity for Chlorobenzene and Chlorocyclohexane Fractionation. *J. Am. Chem. Soc.* **2019**, *141* (31), 12280−12287.
(67) *Glide, V13.2, Release 2023-3*; Schrodinger LLC: New York, NY, 2023.
(68) Kuntz, I. D.; Blaney, J. M.; Oatley, S. J.; Langridge, R.; Ferrin, T. E. A Geometric Approach to Macromolecule-Ligand Interactions. *J. Mol. Biol.* **1982**, *161* (2), 269−288.
(69) Becke, A. D. Density-Functional Thermochemistry. III. The Role of Exact Exchange. *J. Chem. Phys.* **1993**, *98* (7), 5648−5652.
(70) Dolomanov, O. V.; Bourhis, L. J.; Gildea, R. J.; Howard, J. A. K.; Puschmann, H. OLEX2: A Complete Structure Solution, Refinement and Analysis Program. *J. Appl. Crystallogr.* **2009**, *42* (2), 339−341.
(71) Sheldrick, G. Crystal Structure Refinement with SHELXL. *Acta Crystallogr. C* **2015**, *71* (1), 3−8.
(72) Sheldrick, G. A Short History of SHELX. *Acta Crystallogr. A* **2008**, *64* (1), 112−122.
(73) Roos, K.; Wu, C.; Damm, W.; Reboul, M.; Stevenson, J. M.; Lu, C.; Dahlgren, M. K.; Mondal, S.; Chen, W.; Wang, L.; et al. OPLS3e: Extending Force Field Coverage for Drug-Like Small Molecules. *J. Chem. Theory Comput.* **2019**, *15* (3), 1863−1874.
(74) *MacroModel, V12.6, Release 2022-1*; Schrodinger LLC: New York, NY, 2021.
(75) Kamachi, T.; Yoshizawa, K. Low-Mode Conformational Search Method with Semiempirical Quantum Mechanical Calculations: Application to Enantioselective Organocatalysis. *J. Chem. Inf. Model.* **2016**, *56* (2), 347−353.
(76) Lee, C.; Yang, W.; Parr, R. G. Development of the Colle-Salvetti Correlation-Energy formula into a Functional of the Electron Density. *Phys. Rev. B* **1988**, *37* (2), 785−789.
(77) Grimme, S.; Antony, J.; Ehrlich, S.; Krieg, H. A Consistent and Accurate Ab Initio Parametrization of Density Functional Dispersion Correction (DFT-D) for the 94 Elements H-Pu. *J. Chem. Phys.* **2010**, *132* (15), 154104.
(78) Grimme, S.; Ehrlich, S.; Goerigk, L. Effect of the Damping Function in Dispersion Corrected Density functional Theory. *J. Comput. Chem.* **2011**, *32* (7), 1456−1465.
(79) *Gaussian 09*; Wallingford, CT, 2009.
(80) Boys, S. F.; Bernardi, F. The Calculation of Small Molecular Interactions by the Differences of Separate Total Energies. Some Procedures with Reduced Errors. *Mol. Phys.* **1970**, *19* (4), 553−566.
(81) Lu, C.; Wu, C.; Ghoreishi, D.; Chen, W.; Wang, L.; Damm, W.; Ross, G. A.; Dahlgren, M. K.; Russell, E.; Von Bargen, C. D.; et al. OPLS4: Improving Force Field Accuracy on Challenging Regimes of Chemical Space. *J. Chem. Theory Comput.* **2021**, *17* (7), 4291−4300.

https://doi.org/10.1021/jacsau.4c00310
JACS Au 2024, 4, 3475−3483